Journal of Science and Transport Technology
Journal homepage: https://jstt.vn/index.php/en

Influence of cation type on chloride binding and phase assemblage evolution in saturated concrete: A reactive transport approach

Quang Hung Nguyen[1], Tuan Anh Nguyen[2], Duc-Phi Do[3], Van Quan Tran[4], Long Khanh Nguyen[4*]

[1]Thuyloi University, Hanoi 100000, Vietnam

[2]Office of the People's Committee of Nghe An province - No. 03, Truong Thi street, Truong Vinh ward, Nghe An, Vietnam

[3]INSA CVL, Lamé, EA 7494, University Orléans, University Tours, 45100 Orléans, France

[4]Resilience & Innovative Materials for Smart Infrastructures (RIMAS), University of Transport Technology, 54 Trieu Khuc, Hanoi, Vietnam

Article info
Type of article:
Original research paper

DOI:
https://doi.org/10.58845/jstt.utt.2025.en.5.4.156-176

[*]**Corresponding author:**
Email address:
khanhnl@utt.edu.vn

Received: 07/10/2025
Received in Revised Form: 02/12/2025
Accepted: 14/12/2025

Abstract: Chloride-induced corrosion remains one of the main durability concerns for reinforced concrete exposed to marine or de-icing environments. Conventional diffusion-based models often neglect the chemical form of chloride and the role of counter-cations in altering hydrated cement. In practice, chloride transport is a reactive process controlled by simultaneous diffusion, binding, dissolution/precipitation, and pH buffering within the evolving cement matrix. This study investigates how different cations Na^+, K^+, Ca^{2+}, and Mg^{2+} affect chloride ingress, binding, and hydrate stability in saturated concrete. A reactive transport model is developed that couples diffusion, aqueous speciation, mineral equilibrium, kinetic reactions, and surface complexation on C-S-H. The simulations reproduce and extend the experimental results of literature for four boundary solutions: 0.5 mol/l NaCl, 0.5 mol/l KCl, 0.25 mol/l $CaCl_2$, and 0.25 mol/l $MgCl_2$, over exposure periods up to ten years in saturated concrete. Under NaCl and KCl, the pore network remains stable, alkalinity is maintained, and binding is moderate producing deep free-chloride penetration. Under $CaCl_2$ and $MgCl_2$, strong near-surface reactions occur: AFm phases convert into Kuzel-type compounds, and portlandite dissolution with C-S-H decalcification produces brucite or M-S-H. These transformations trap chloride near the surface, limit transport, and reduce pH in the outer zone. Consequently, monovalent salts lead to transport-controlled ingress, while divalent salts cause binding/microstructure-controlled accumulation. Reliable prediction of corrosion risk requires evaluating free chloride, total chloride, and alkalinity together. Reactive transport modeling thus provides a physically consistent and predictive framework for performance-based durability design of concrete under diverse chloride environments.

Keywords: Chloride ingress, Reactive transport modeling, Cation effect, Phase assemblage, Chloride binding, Concrete durability.

1. Introduction

Corrosion of reinforcing steel caused by chloride ingress is one of the most common and severe forms of deterioration in reinforced concrete exposed to marine or de-icing environments [1]. When chloride ions reach the reinforcement surface, they destroy the passive oxide film on steel and trigger localized corrosion, leading to cracking, spalling, and eventual loss of load-bearing capacity. Understanding how chloride migrates through concrete and interacts with the cement hydrates is thus essential for predicting service life and designing durable structures [2], [3], [4].

Chlorides in cementitious materials exist in two distinct forms: free chloride, which is dissolved in the pore solution and electrochemically active, and bound chloride, which is fixed by physical adsorption, ion exchange, or chemical substitution within hydration products [5]. The free fraction controls the electrochemical risk of steel depassivation, while the bound fraction acts as a reservoir that can release chloride when pH decreases or when equilibrium conditions shift [6]. The partitioning between free and bound chloride depends on the chemical composition of pore solution, the composition of hydrates such as AFm and C-S-H, and the identity of the counter-cation associated with the chloride salt [7].

Earlier research on chloride ingress typically assumed that diffusion could be represented by Fick's law with a time-independent diffusion coefficient [8], [9]. Binding was often modeled empirically using Freundlich or Langmuir isotherms, neglecting the coupling between transport, dissolution/precipitation reactions, and microstructural evolution [10], [11]. However, several studies have shown that chloride transport in cementitious materials is a reactive process rather than purely diffusive [12]. Dissolution of portlandite, transformation of AFm to Friedel's or Kuzel's salt, and decalcification of C-S-H all alter the pore structure, permeability, and alkalinity, thereby affecting subsequent chloride mobility [13], [14].

Moreover, the cation type accompanying chloride has been demonstrated to have a substantial influence on both transport and binding. Song et al. [15] compared the diffusion of NaCl, KCl, $CaCl_2$, and $MgCl_2$ in ordinary Portland cement concrete and found that the chloride penetration depth decreased in the order KCl ≈ NaCl > $CaCl_2$ > $MgCl_2$. Li et al. [16] reported that chloride binding isotherms and diffusion coefficients differ markedly among chloride salts even at equal molar Cl^- concentrations. Chen and Ye [17] also confirmed that magnesium exposure promotes decalcification of C-S-H and portlandite depletion, leading to lower pH and reduced buffering capacity of the paste.

These findings indicate that chloride ingress cannot be generalized solely by the total chloride content or diffusion coefficient; it must also account for the reactive coupling between chloride transport, mineral transformation, and pore solution chemistry. To address this, recent advances have introduced reactive transport models that integrate multi-ionic diffusion, aqueous speciation, thermodynamic equilibria, kinetic mineral reactions, and surface complexation on C-S-H [2], [7], [18], [19]. Such models can simulate both the evolution of free and bound chloride and the associated changes in porosity and pH over time, enabling a physically consistent prediction of corrosion risk.

The present study applies this reactive transport approach to simulate chloride ingress in saturated concrete under four boundary chloride solutions: 0.5 mol/l NaCl, 0.5 mol/l KCl, 0.25 mol/l $CaCl_2$, and 0.25 mol/l $MgCl_2$. The model couples Fickian transport with phase-equilibrium and kinetic reactions for AFm/Friedel transformations, portlandite consumption, and C-S-H decalcification, while explicitly accounting for chloride binding through surface complexation. Model results are compared with long-term experimental data from Song et al. [15] and other relevant studies, evaluating both free and total chloride profiles over exposure durations from six

months to ten years.

The objectives of this paper are threefold:

1. To quantify how cation type influences chloride transport and binding in saturated concrete.

2. To elucidate the phase-assemblage evolution and associated changes in alkalinity and porosity.

3. To demonstrate the potential of reactive transport modelling as a predictive and diagnostic tool for performance-based durability design.

Ultimately, this study highlights that the chemical nature of the chloride source particularly the boundary cation governs the balance between diffusion, binding, and microstructural change, and therefore must be considered explicitly in both modeling and design for chloride-induced corrosion.

2. Theoretical basis of the reactive transport model

In this study, the reactive transport of chloride in saturated concrete is simulated with TOUGHREACT [20]. The framework couples mass conservation, Fickian diffusion, thermodynamic equilibrium (dissolution/precipitation and aqueous complexation), surface complexation, and reaction kinetics for cement hydration phases.

The mass balance for an aqueous species *j* in the pore solution is:

$$\frac{\partial(\phi C_j)}{\partial t} = \nabla(\tau\phi D_e \nabla C_j) + q_j \quad (1)$$

where C_j (mol.m^{-3}) is the molar concentration of species j, D_e (m^2.s^{-1}) the effective diffusion coefficient, q_j (mol.m^{-}3.s^{-1}) the net source/sink due to adsorption on C-S-H, mineral reactions, and aqueous complexation, and ϕ the porosity.

According to Xu et al. [20], the effective diffusivity depends on porosity and tortuosity:

$$D_e = \frac{D_{j,w}}{\phi\tau} \quad (2)$$

with $D_{j,w}$ the diffusivity of species *j* in free water and τ the tortuosity factor. D_e= 2×10^{-12} m^2/s is the effective diffusion coefficient of species j in ordinary concrete; the value is the same for all species [2]. Porosity evolves with mineral dissolution/precipitation according to Steefel et al. [21]:

$$\frac{d\phi}{dt} = -\sum_m \frac{1}{\rho_m}\frac{dV_m}{dt} \quad (3)$$

where V_m and ρ_m are the volume fraction and density of mineral mmm. Consequently, changes in mineralogy feed back into both ϕ and D_e, coupling chemistry and transport in the saturated matrix.

Under thermodynamic equilibrium, the saturation state of a mineral mmm is described by:

$$\Omega_m = \frac{\prod_j a_j^{\nu_{m,j}}}{K_{s,m}}$$
$$a_j = \gamma_j C_j \quad (4)$$
$$IS_m = \log\Omega_m$$

where $K_{s,m}$ is the equilibrium constant, $\nu_{m,j}$ the stoichiometric coefficient, γ_j the activity coefficient, and IS_m the saturation index (IS_m =0 equilibrium, IS_m <0 undersaturation or dissolution, IS_m > 0 supersaturation or precipitation). Equilibrium data for the cement-seawater system (Portlandite, C-S-H, AFt/AFm, Hydrotalcite, Friedel-related phases, etc.) are taken from the database developed by Tran [5], ensuring consistency across transport, equilibrium, and kinetic modules.

Equilibrium alone cannot capture rate-dependent evolution over short or transient exposures. We therefore include mineral kinetics, noting that thermodynamic and kinetic predictions converge only after long alteration (10 years) in analogous interfaces [22], whereas months-years require kinetic control and many reactions (e.g., metastable C-S-H or quartz) are slow and quasi-irreversible [23]. Following Lasaga et al. [24], the dissolution/precipitation rate of mineral m is:

$$r_m = k_m A_{ms}(1-\Omega_m)^{\eta} \quad (5)$$

with r_m positive for dissolution and negative for precipitation, k_m the intrinsic rate constant, A_{ms} the

specific reactive surface area ($m^2.g^{-1}$), and η≈1. Temperature dependence follows Arrhenius:

$$k_m(T) = k_{25,m}\exp\left[-\frac{E_a}{R}\left(\frac{1}{T}-\frac{1}{298.15}\right)\right] \quad (6)$$

where $k_{25,m}$ is the rate constant at 25 °C, E_a the activation energy, R the gas constant, and T the absolute temperature. Kinetic parameters are from Baur et al. [25] for Monosulfoaluminate, Ettringite, and C-S-H (Jennite, Tobermorite) [10]; and Palandri & Kharaka [26] for Brucite. Hydrotalcite and Kuzel salt are treated as instantaneous (equilibrium-controlled). Table 1 shows the thermodynamic reactions, equilibrium constant and kinetic parameters for dissolution/precipitation mineral of cement-chloride solution system at 25°C.

The thermodynamic equilibrium constants and kinetic reference parameters listed in Table 1 correspond to the standard database values at 25 °C; in the simulations, these constants are internally recalculated by TOUGHREACT at the working temperature of 21°C using the built-in temperature-dependence relations for log K(T) (cf. equation 7) and the Arrhenius law for reaction rates (cf. equation 6).

$$\log(K_s)_T = c_0\ln(T_K) + c_1 + c_2T_K + \frac{c_3}{T_K} \quad (7)$$

where c_0, c_1, c_2 and c_3 are the constant parameters to be available in thermodynamic database of Blanc et al. [27], Tran [5] and Tran et al. [2], [7]. The thermodynamic database employed in this study is a TOUGHREACT-compatible input file compiled from published datasets for cementitious systems [2], [5], [7], [27], the complete file is available from the corresponding author upon reasonable request to facilitate reproducibility.

Table 1. Thermodynamic reactions and kinetic parameters for dissolution/precipitation mineral of cement-chloride solution system (25°C)

Mineral	Reaction of mineral in solution	$\log K_{25°C}$	k(mol/m²/s)	A_{ms} (m²/g)
Jennite	$(CaO)_{1.67}(SiO_2).(H_2O)_{2.1} + 2.33H^+ \leftrightarrow 1.67Ca^{2+} + HSiO_3^- + 2.76H_2O$	19.53	2.75×10^{-12}	41
Tobermorite	$0.83Ca^{2+} + HSiO_3^- + 1.16H_2O \leftrightarrow 0.83Ca^{2+} + HSiO_3^- + 1.16H_2O$	0.63	2.75×10^{-12}	41
Portlandite	$Ca(OH)_{2(s)} + 2H^+ \leftrightarrow Ca^{2+} + 2H_2O$	22.76	7.08×10^{-13}	9.8
Monosulfoaluminate	$Ca_4Al_2SO_4(OH)_{12}.6H_2O + 12H^+ \leftrightarrow 4Ca^{2+} + 2Al^{3+} + SO_4^{2-} + 18H_2O$	72.44	6.76×10^{-12}	5.7
Ettringite	$Ca_6Al_2(SO_4)_3(OH)_{12}.26H_2O + 12H^+ \leftrightarrow 6Ca^{2+} + 2Al^{3+} + 3SO_4^{2-} + 38H_2O$	56.67	2.75×10^{-12}	41
Hydrotalcite	$Mg_4Al_2(OH)_{14}.3H_2O + 14H^+ \leftrightarrow 4Mg^{2+} + 2Al^{3+} + 17H_2O$	74.68	Instantaneous	
Kuzel's salt	$Ca_4Al_2(SO4)_{0.5}Cl(OH)_{12}.6H_2O + 12H^+ \leftrightarrow 4Ca^{2+} + 2Al^{3+} + 0.5SO_4^{2-} + Cl^- + 18H_2O$	73.24	Instantaneous	
Brucite	$Mg(OH)_{2(s)} + 2H^+ \leftrightarrow Mg^{2+} + 2H_2O$	17.11	3.16×10^{-12}	9.8×10^{-4}
Sepiolite	$Mg_4Si_6O_{15}(OH)_2.6H_2O + 2H^+ \leftrightarrow 4Mg^{2+} + 6HSiO_3^- + 8H_2O$	-29.01	Instantaneous	

Finally, surface complexation on C-S-H governs chloride binding/release. Ions (Ca^{2+}, K^+, Na_+, Cl^- diffuse through the pore concrete and react at ≡SiOH sites on C-S-H. Specific adsorption ion

reactions are modeled by the law of mass action (with electrostatic correction):

$$K_{eq} = \frac{[\equiv SiOHCaCl][H+]}{[\equiv SiOH][Ca2+][Cl-]} \exp(-\frac{F\psi_0}{RT}) \quad (8)$$

where F is the Faraday constant and ψ_0 the surface potential. Equilibrium constants for hydroxylation and Cl^- adsorption/desorption on C-S-H are from Tran et al. [7], enabling a consistent coupling of mineral transformation kinetics and surface complexation equilibria with transport capturing both the physical ingress and chemical binding of chloride in the cementitious matrix. Equilbrium constant of surface adsorption reactions on C-S-H is shown in Table 2.

Table 2. Surface adsorption reactions on C-S-H and equilibrium constants at 21°C [18]

Surface adsorption reactions	log(K)
$\equiv SiOH \leftrightarrow \equiv SiO^- + H^+$	-12.83
$\equiv SiOH + Ca^{2+} \leftrightarrow \equiv SiOCa^+ + H^+$	-9.44
$\equiv SiOH + Cl^- \leftrightarrow SiOHCl^-$	-0.385
$\equiv SiOH + Ca^{2+} + Cl^- \leftrightarrow \equiv SiOCaCl + H^+$	-9.83
$\equiv SiOH + Ca2^+ + SO_4^{2-} \leftrightarrow \equiv SiOCaSO_4^- H^+$	-8.56
$\equiv SiOH_{jennite} + Na^+(K^+) \leftrightarrow \equiv SiONa(K) + H^+$	-13.8
$\equiv SiOH_{tobermorite} + Na^+ (K^+) \leftrightarrow \equiv SiONa(K) + H^+$	-12.845
Specific surface area of C-S-H: A_{cs} =500 m^2/g	
Surface site density C-S-H $\delta_{CSH}=8\times10^{-6}$ mol/m^2	

3. Materials, Boundary Chemistry, and Numerical Setup

The problem is posed as one-dimensional diffusion in a fully saturated concrete, consistent with the configuration of Song et al. [15] and the schematic in Figure 1. The computational domain is L = 100 mm, discretized into 1000 uniform cells (Δx=0.1 mm). The exposed face (x=0) is a fixed-composition (Dirichlet) reservoir; the interior face (x= L) is no-flux (Neumann). Transport is diffusion-controlled (no advection) and, isothermal at 21°C to match the boundary speciation.

The starting mineral assemblage and pore solution were obtained by dynamic equilibrium with GEMS (Gibbs Energy Minimization Software) following Kulik et al. [28] assuming a stabilized CEM II paste. The resulting hydrated phases such as Portlandite, Hydrotalcite, Monosulfoaluminate (AFm), and C-S-H (Jennite, Tobermorite) and the corresponding pore-solution composition are listed in Table 3. Secondary phases (Ettringite, Kuzel's salt, Brucite, Sepiolite) are set to zero at t=0 but are allowed to precipitate/dissolve during exposure.

To interrogate counter-cation effects at fixed chloride level, the exposed face is alternately contacted with 0.50 mol/l NaCl, 0.50 mol/l KCl, 0.25 mol/l $CaCl_2$, and 0.25 mol/l $MgCl_2$. Full aqueous speciation (charge balance, complexation) is enforced in Toughreact for each electrolyte; the resulting ion inventories and pH used at the boundary are summarized in Table 4. These Dirichlet conditions remain constant throughout each run.

Diffusion of all aqueous species uses a uniform effective diffusivity $De=2\times10^{-12}$ $m^2.s^{-1}$ for ordinary concrete [2]. Porosity ϕ(t,x) evolves locally with mineral dissolution/precipitation (Steefel et al. [21]) and updates the transport properties through the adopted tortuosity-porosity relation. Thermodynamic data for dissolution/precipitation and complexation of cement phases (Portlandite, C-S-H, AFt/AFm, Hydrotalcite, Kuzel salt-related phases, etc.) follow the cement-seawater database compiled by Tran [5] and Tran et al. [2], [7]. Kinetic parameters are from Baur et al. [25] (Monosulfoaluminate, Ettringite, C-S-H), Galí et al. [29] (Portlandite, Hydrotalcite), and Palandri and Kharaka [26] (Brucite); fast ion-exchange phases (e.g., Kuzel's salt) are treated at equilibrium. Surface complexation on C-S-H governs chloride

binding/release using mass-action expressions with electrostatic correction and constants after Tran et al. [18].

Model outputs comprise depth profiles of free chloride and total chloride (free + bound by minerals/surface sites), pH, porosity, and mineral volume fractions. For model validation against Song et al. [15], simulated free/total chloride profiles are extracted at 0.5 year, 2 years, 5 years, and 10 years and compared to the corresponding experimental profiles for each electrolyte. This validation briefly recalled here anchors the transport-reaction description; the same runs are then exploited to analyze how Na^+, K^+, Ca^{2+}, and Mg^{2+} modulate the mineralogical evolution of the concrete over 10 years (Portlandite depletion, AFt/AFm transformation, formation of Kuzel's salts, Hydrotalcite and Mg-silicates), thereby clarifying counter ion specific impacts under identical chloride loading.

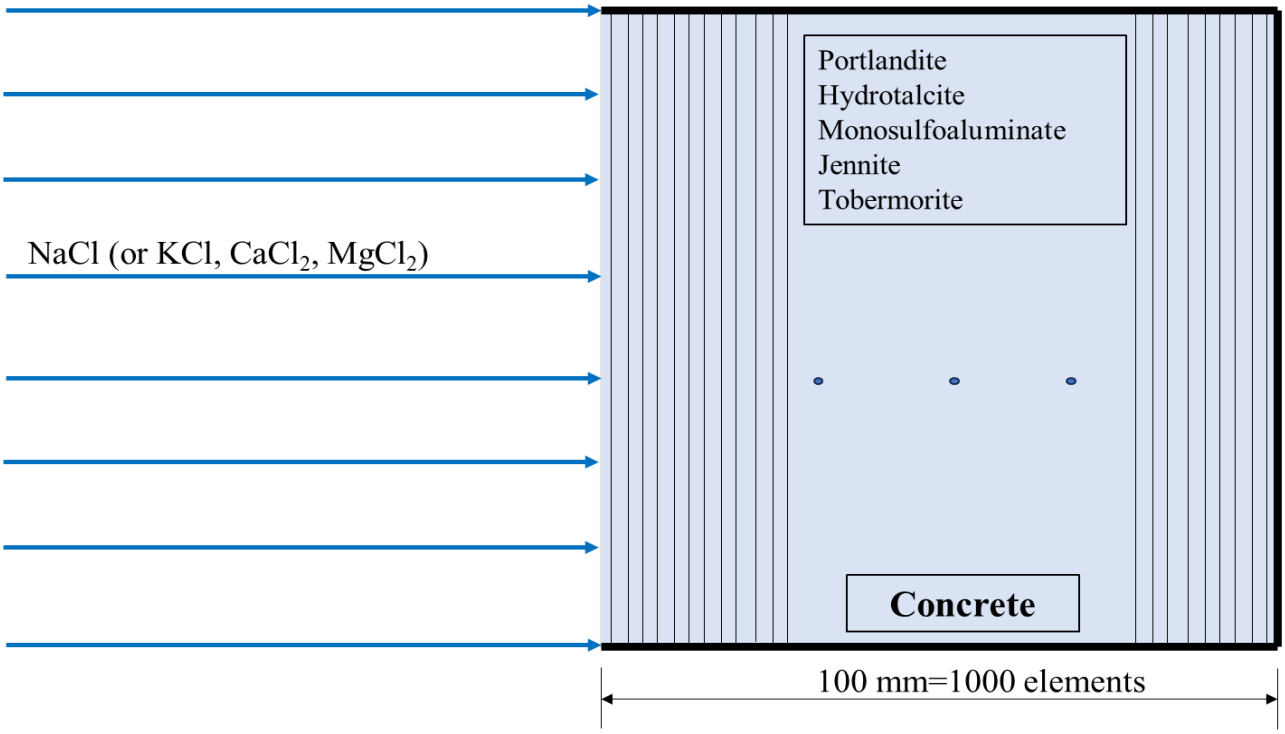

Figure 1. Schematic of concrete exposed to different chloride solutions

Table 3. Initial hydrated mineral composition of concrete (mol/dm³ of concrete) and initial pore solution of concrete (mol/ litre of solution)

Minerals		Content	Ion	Concentration (mol/kg of pore solution)
Initial Phases	Jennite	0.099	Na^+	0.14
	Tobermorite	0.014	K^+	0.23
	Monosulfoaluminate	0.040	Ca^{2+}	0.30×10^{-2}
	Portlandite	1.600	Mg^{2+}	0.41×10^{-10}
	Hydrotalcite	0.020	Al^{3+}	0.24×10^{-4}
			$HSiO_3^-$	0.16×10^{-3}
Secondary Phases	Ettringite	0		
	Kuzel	0	SO_4^{2-}	0.2×10^{-4}
	Brucite	0	pH	13.5
	Sepiolite	0		

Table 4. Concentration of boundary chloride solutions

Ion	NaCl solution (mol/l)	KCl solution (mol/l)	$CaCl_2$ solution (mol/l)	$MgCl_2$ solution (mol/l)
Na^+	0.5	-	-	-
K^+	-	0.5	-	-
Ca^{2+}	-	-	0.25	-
Mg^{2+}	-	-	-	0.25
Cl^-	0.5	0.5	0.5	0.5
pH	8.10	8.05	11.71	9.55

4. Results and Discussion

4.1. Model Validation under saturated condition

Figure 2 compares simulated depth profiles of free and total chloride with the measurements of Song et al. [15] after 6 months of full immersion (fully saturated conditions**)** in four electrolytes: (a) 0.5 mol/l NaCl, (b) 0.5 mol/l KCl, (c) 0.25 mol/l $CaCl_2$, and (d) 0.25 mol/l $MgCl_2$. Across all cases, the model reproduces the monotonic decay with depth and the separation between free and total contents. The free chloride content curves track the data closely over 0-25 mm, while the total chloride predictions capture both magnitude and slope, indicating consistent representation of chloride binding by AFm/Kuzel-type phases and surface complexation on C-S-H.

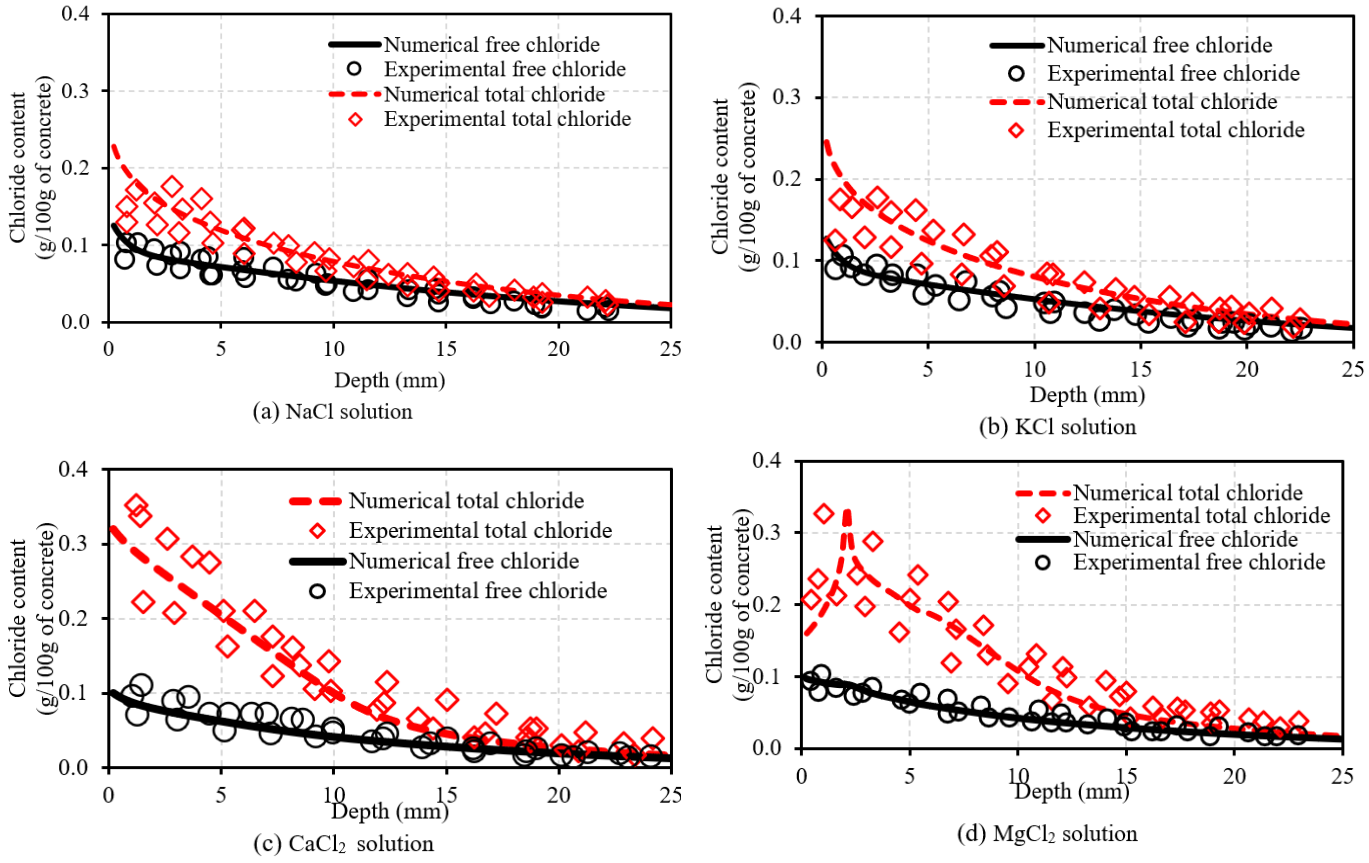

Figure 2. Comparison between simulated and experimental free and total chloride profiles in saturated concrete after 6 months of immersion in NaCl, KCl, $CaCl_2$ and $MgCl_2$ solutions published in previous study [30]

Minor deviations appear in the first 2-4 mm, the differences may be explained by: (i) the model assuming a constant chloride concentration at the surface, while in reality a thin diffusion layer forms in the solution;(ii) small changes in porosity or tortuosity near the surface due to casting effects;

(iii) measurement errors when separating “free” and “total” chloride at high salt levels; and (iv) the model using simple Fickian diffusion without accounting for ion-ion interactions or electric effects, which can slightly affect chloride movement near the surface.

Beyond ~5-7 mm, agreement is very good for all four electrolytes. Crucially, no parameter re-tuning was required between different solutions, only the boundary chemistry was changed supporting the robustness of the reactive transport model for predicting both free and total chloride profiles and providing a solid basis for the subsequent mineralogical analysis up to 10 years.

4.2. Chloride ingress into the concrete for long term

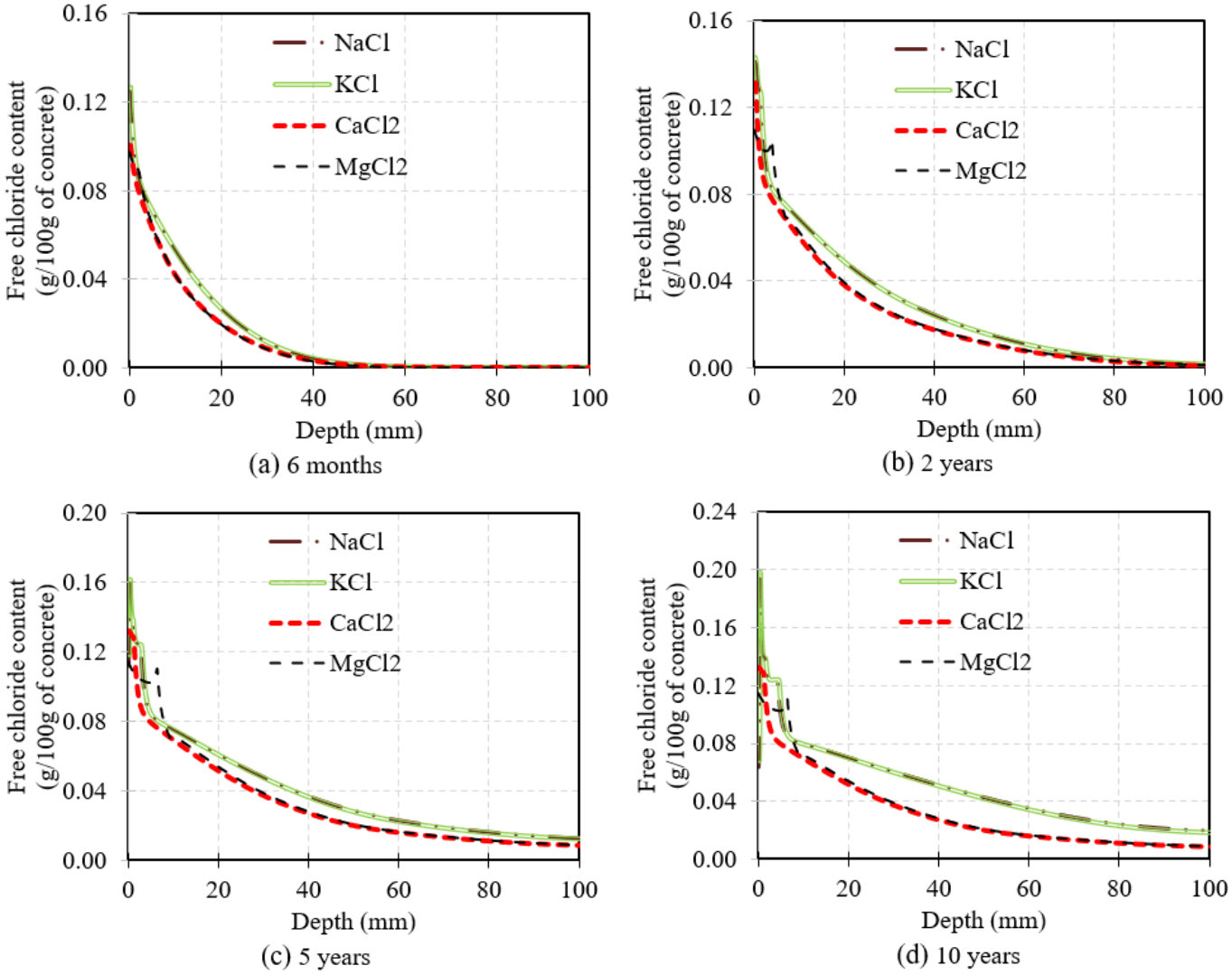

Figure 3. Free chloride content over depth of concrete exposed to different chloride solutions from 6 months to 10 years

Chloride ingress from 6 months to 10 years was evaluated under four boundary solutions: 0.5 mol/l NaCl, 0.5 mol/l KCl, 0.25 mol/l $CaCl_2$, and 0.25 mol/l $MgCl_2$. These conditions were taken from the experimental program of Song et al. [15]. Two indicators were considered at the same time: free chloride, which governs steel depassivation, and total chloride (free + bound), which represents a reservoir that may be released when pH declines [31]. Results for free Cl^- are shown in Figure 3, and results for total Cl^- are shown in Figure 4.

A common shape was predicted for all solutions. Surface maxima at 0-5 mm were followed by non-linear declines with depth, which is typical of diffusion with binding in saturated concrete [32]. As exposure increased from 6

months to 10 years, the iso-concentration fronts moved inward. Thus, the penetration depth grew with time. Monovalent salts (NaCl, KCl) produced deeper chloride penetration than divalent salts ($CaCl_2$, $MgCl_2$) causing heavy near-surface accumulation and steep attenuation at depth. This behavior is consistent with stronger chemical fixation and microstructural alteration in Ca^{2+}/Mg^{2+} environments [33].

For free chloride (Figure 3), a consistent order was obtained at mid-depth (≈30-80 mm): KCl ≳ NaCl ≫ $CaCl_2$ > $MgCl_2$. At 6 months, the difference between NaCl and KCl was small. By 2-5 years, a longer and more persistent tail was formed under KCl than under NaCl. By 10 years, measurable free Cl^- remained at ~80-100 mm for NaCl/KCl, while near-zero free Cl^- was reached for $CaCl_2$/$MgCl_2$ at those depths. This response is consistent with weaker specific binding under monovalent cations and with less disruption of effective diffusivity when the pore structure is not strongly altered by divalent reactions [33]. The trend agrees with the saturated-immersion observations of Song et al. [15].

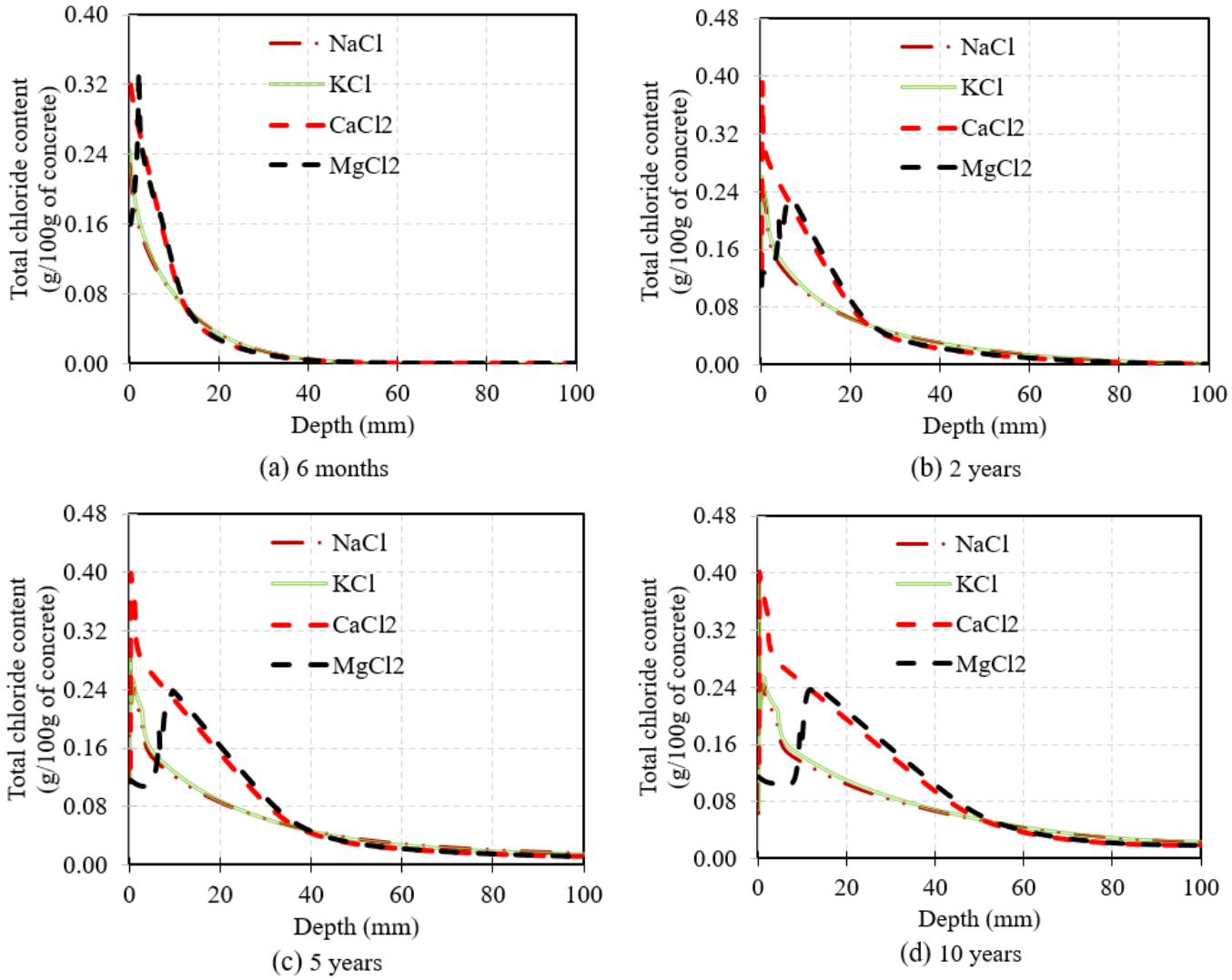

Figure 4. Total chloride content over depth of concrete exposed to different chloride solutions from 6 months to 10 years

For total chloride (Figure 4), $CaCl_2$ and $MgCl_2$ produced much higher totals at 5-15 mm (≈0.30-0.45 g/100 g). These high near-surface values stayed stable or rose slightly with time, and then dropped rapidly with depth. Under $CaCl_2$, AFm phases were converted toward Kuzel type compounds, which fix chloride strongly near the exposed face. Under $MgCl_2$, brucite and Mg-

silicate-hydrate (M-S-H) formed, and the surface structure changed. These effects created chemical and geometric traps that held chloride close to the boundary [9]. In contrast, NaCl/KCl showed lower totals at the face but extended farther into the cover, which matched their higher free Cl^- at depth.

A practical threshold of 0.04g/100g of concrete was adopted for free chloride at the bar level [31]. This choice lies within the ranges summarized in the literature and is consistent with conversions from the Hausmann concept when alkalinity is considered [34]. Using this threshold, the 10-year penetration depth ranked KCl ≈ NaCl > $CaCl_2$ > $MgCl_2$. This order cannot be inferred from total chloride alone. $CaCl_2$/$MgCl_2$ generated very high totals near the surface, but this did not imply early depassivation if the cover was sufficient. Conversely, NaCl/KCl, which showed lower totals at the surface, pushed free chloride deeper and reduced the passive-film safety margin sooner.

At 6 months, steep profiles were seen for all solutions, and differences were concentrated in 0-20 mm. $CaCl_2$/$MgCl_2$ showed higher total and lower free chloride near the face. At 2 years, stable free-chloride tails to ~40-60 mm were present for NaCl/KCl, while $CaCl_2$/$MgCl_2$ remained surface-dominated. At 5 years, the split widened: free Cl^- for NaCl/KCl at 50-80 mm clearly exceeded $CaCl_2$/$MgCl_2$, and total Cl^- for $CaCl_2$/$MgCl_2$ peaked with a very sharp 0-15 mm gradient [15], [33]. At 10 years, the same ordering persisted. Free Cl^- for NaCl/KCl was still detectable toward ~100 mm, while $CaCl_2$/$MgCl_2$ continued to dominate total near the face with limited impact at depth.

Several implications follow for corrosion assessment. First, free chloride should be used as the primary metric to time corrosion initiation at steel depth. Reliance on total chloride alone can cause misjudgment when the boundary counter-ion changes from Na^+/K^+ to Ca^{2+}/Mg^{2+}. Second, the counter-ion identity governs the transport reactive coupling. Monovalent boundaries lead to a transport-controlled regime and deeper ingress. Divalent boundaries lead to a binding/microstructure-controlled regime with strong near-surface fixation. Third, earlier depassivation steel should be expected under thin covers or NaCl/KCl exposure. Under $CaCl_2$/$MgCl_2$, outer-layer alkalinity loss, local porosity changes, and surface weakening should be monitored as an indirect path to later corrosion through chloride release [35].

A brief regulatory note is needed. Interpretation against code limits should distinguish total and free chloride. The EN 206 [36] limit on total chloride by binder mass (≈0.20-0.40 %) is widely cited. However, conversion to concrete mass and to free chloride at steel depth is mix-dependent and non-trivial. Therefore, the use of $[Cl^-]/[OH^-]$ or a validated free-chloride threshold at the bar level is recommended for service-life checks [6]. The Hausmann [34] criterion ($\approx[Cl^-]/[OH^-] \approx 0.6$) remains a practical reference, provided that the local alkalinity is captured by the model [1].

In summary, Figures 3-4 support two distinct ingress regimes. Under NaCl/KCl, deep ingress with elevated free Cl^- at mid-cover was obtained. Earlier depassivation should be expected unless effective diffusivity and pore connectivity are reduced [2]. Under $CaCl_2$/$MgCl_2$, strong near-surface accumulation linked to mineral and pH changes (AFm forming Kuzel/Friedel, brucite) was produced (cf. next section). The outer layer may weaken, and a long-term chloride reservoir may form that can be released as alkalinity declines [35]. For this reason, service-life analyses should apply the free chloride content (and, ideally, $[Cl^-]/[OH^-]$ at steel depth) for the specific boundary solution, rather than a single generic surface limit on total chloride.

4.3. Pore solution alkalinity and porosity evolution

Figure 5 tracks pore-solution pH with depth and time for four boundary solutions (0.5 mol/l NaCl, 0.5 mol/l KCl, 0.25 mol/l $CaCl_2$, 0.25 mol/l $MgCl_2$). Figure 6 shows the matching porosity fields. Together, these fields explain the free/total

chloride profiles in Figures 3-4 (cf. 4.2). High alkalinity is preserved in the inner cover at early ages, while the surface zone loses pH and the front moves inward with time. The strongest near-surface pH loss occurs with divalent solutions ($CaCl_2$, $MgCl_2$). Under $MgCl_2$, portlandite is consumed and C-S-H is decalcified and partly converted, so buffering capacity drops. Under $CaCl_2$, pH loss is milder than with $MgCl_2$ but still larger than with NaCl/KCl, driven by ion exchange and AFm transformations near the face. NaCl/KCl keep higher pH at mid-cover, which aligns with deeper free-chloride tails at later times (cf. 4.2). This matters for corrosion: higher $[OH^-]$ (higher pH) delays depassivation; sustained pH loss raises the $[Cl^-]/[OH^-]$ ratio at bar depth even if free chloride is unchanged [35].

Porosity changes are small near the face at short times and grow with exposure (Figure 6). Two patterns are clear. With NaCl/KCl, mineral alteration is limited, pore connectivity is less disturbed, and effective diffusivity stays relatively high. This allows deeper transport of free Cl^-, consistent with Figure 3. With $CaCl_2/MgCl_2$, reactions near the face modify the solid phase. Local dissolution (e.g., portlandite) and re-precipitation can co-exist, but the net effect is a larger change in the outer millimeters. Under $MgCl_2$, outer-zone decalcification is most evident, which weakens alkalinity and can alter connectivity, consistent with the investigation of De Weerdt et al. [35].

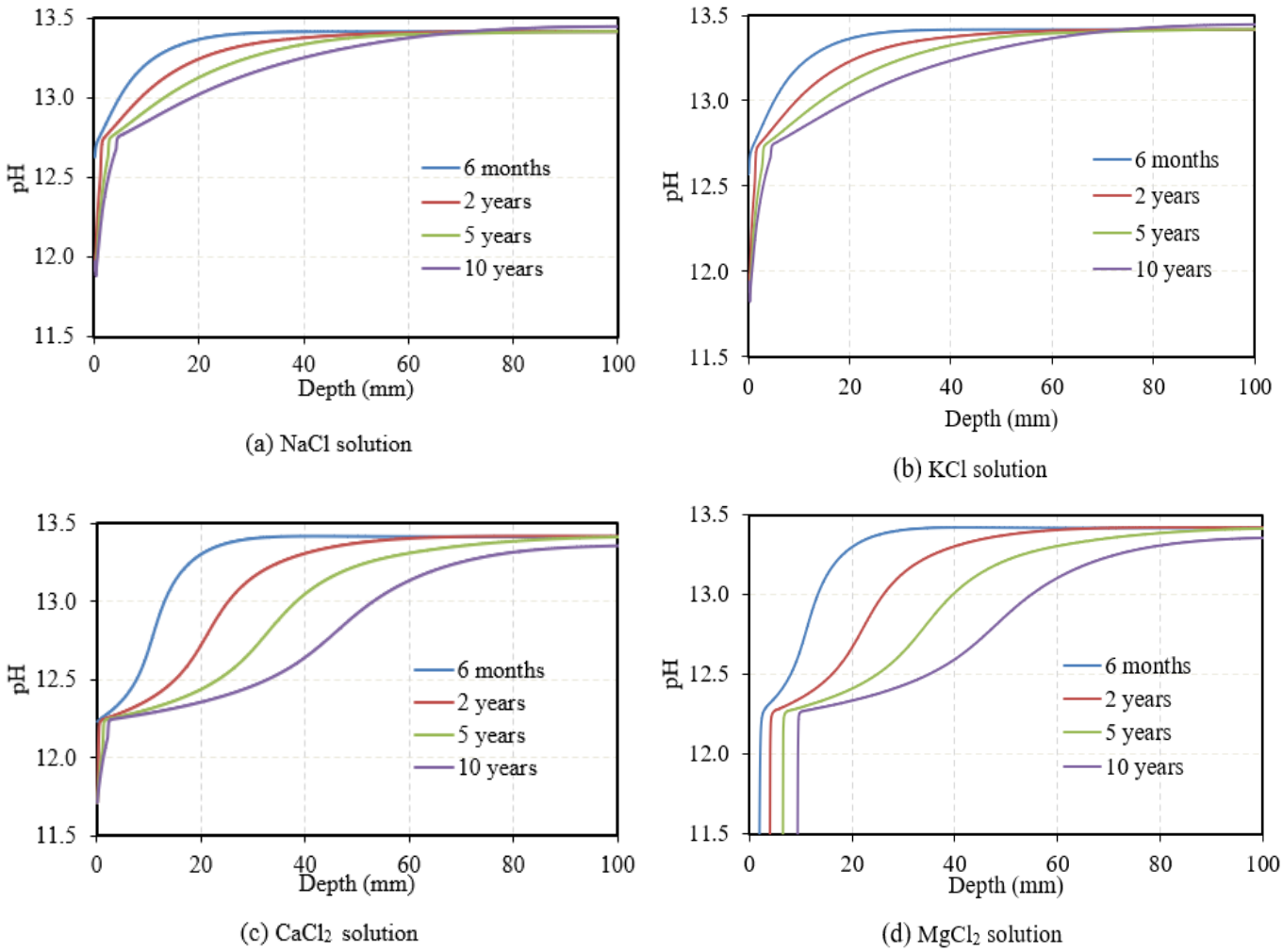

Figure 5. pH over depth of concrete exposed to different chloride solutions from 6 months to 10 years

These pH and porosity maps explain the ingress regimes in section 4.2. NaCl/KCl produce deep free-chloride tails, so the process is transport-controlled. $CaCl_2/MgCl_2$ yield high totals at the face

and a sharp fall with depth, so the process is binding/microstructure-controlled. For assessment, the bar-level free-chloride threshold (0.04 g/100 g concrete) should be checked with local pH and porosity evolution. The patterns match saturated-immersion observations reported by Song et al. for different chloride cations [15].

The implication for risk at 50 mm cover is direct. Under NaCl/KCl, escalation of reinforcement depassivation is governed by transport because pH is maintained and pores remain connected. Under $CaCl_2$/$MgCl_2$, escalation of reinforcement depassivation is indirect because pH loss and phase change in the outer zone can later release chloride toward the bar. In both cases, the timing of depassivation depends on the joint evolution of free chloride, total chloride (as a reservoir), and alkalinity at the steel depth.

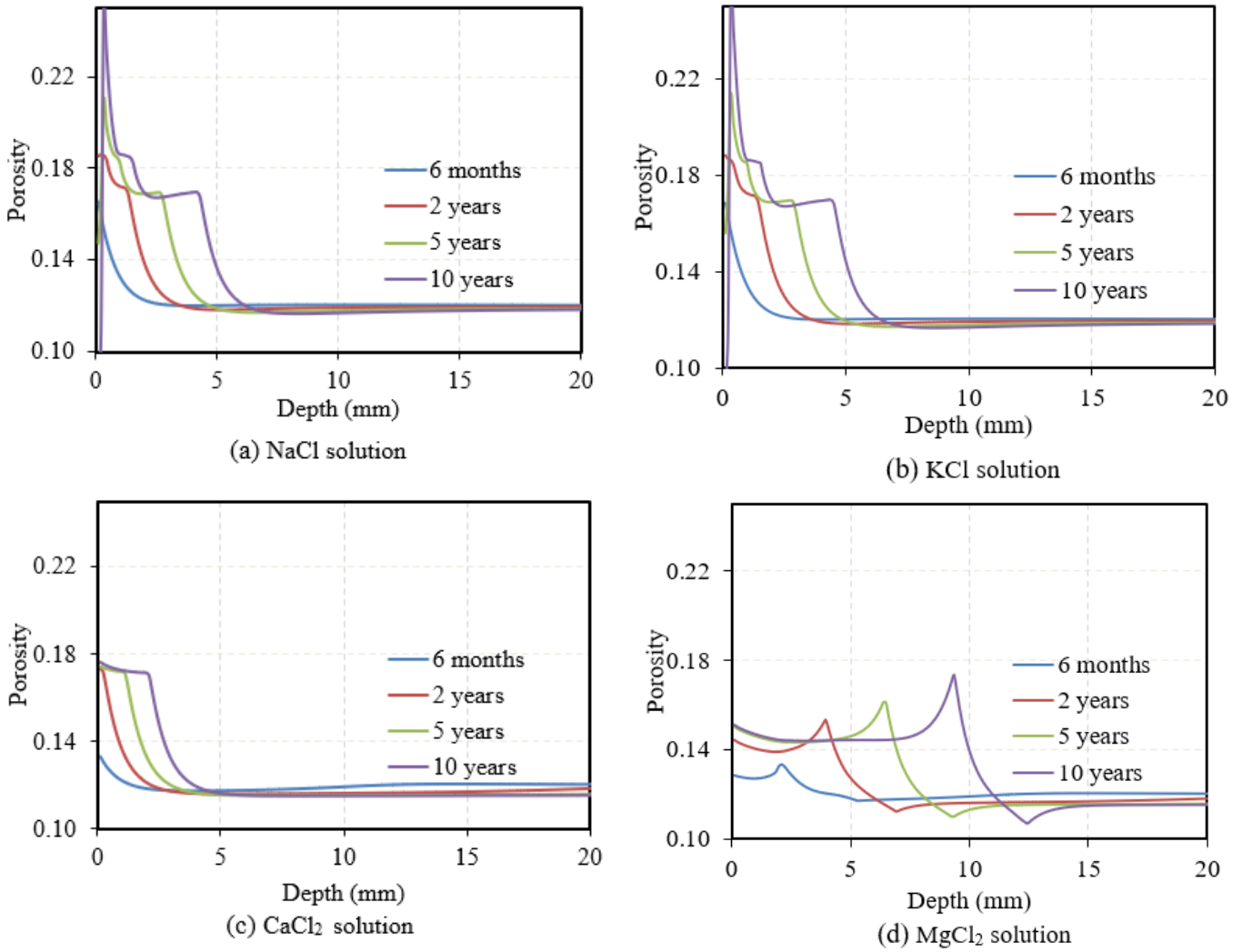

Figure 6. Porosity over depth of concrete exposed to different chloride solutions from 6 months to 10 years

4.4. Phase-assemblage transformations

Figures 7-13 show how the solid phases change with time and depth under the four boundary solutions, and how these changes control chloride binding. These transformations determine how much chloride is fixed or mobile, how the porosity evolves, and how the pore solution is buffered. The trends should be read together with the ingress fields in Figures 3-4 and the pH/porosity maps in Figures 5-6.

Figure 7 shows that Portlandite remains nearly stable under NaCl, KCl, and $CaCl_2$, with only minor dissolution near the exposed face. Under $MgCl_2$, however, portlandite is strongly depleted within the first 10 mm, marking the onset of decalcification and pH loss. Hydrotalcite (cf. Figure 8) shows similar stability in monovalent systems but partial breakdown in $MgCl_2$, confirming that

Mg^{2+} reduces buffering capacity.

AFm like Monosulfoaluminate salt and Aft like Ettringite (Figures 9-10) exhibit the most reactive behavior. AFm decreases markedly near the surface, especially under $CaCl_2$ and $MgCl_2$, reflecting the formation of chloride-bearing phases such as Kuzel salts increasing total chloride content at near surface (cf. Figure 4). In contrast, ettringite precipitates progressively, particularly in divalent environments, through sulfate-chloride exchange. This coupled transformation concentrates chloride binding in the outer zone while accelerating local alkalinity loss.

C-S-H including Jennite and Tobermorite derivatives (Figures 11-12) remain essentially unchanged under NaCl, KCl, and $CaCl_2$, confirming the stability of the silicate backbone. In $MgCl_2$, both dissolve within the top 5-10 mm and are replaced by Mg-silicate-hydrate (M-S-H as Sepiolite), which binds chloride poorly and reduces the pH of the surrounding pore solution.

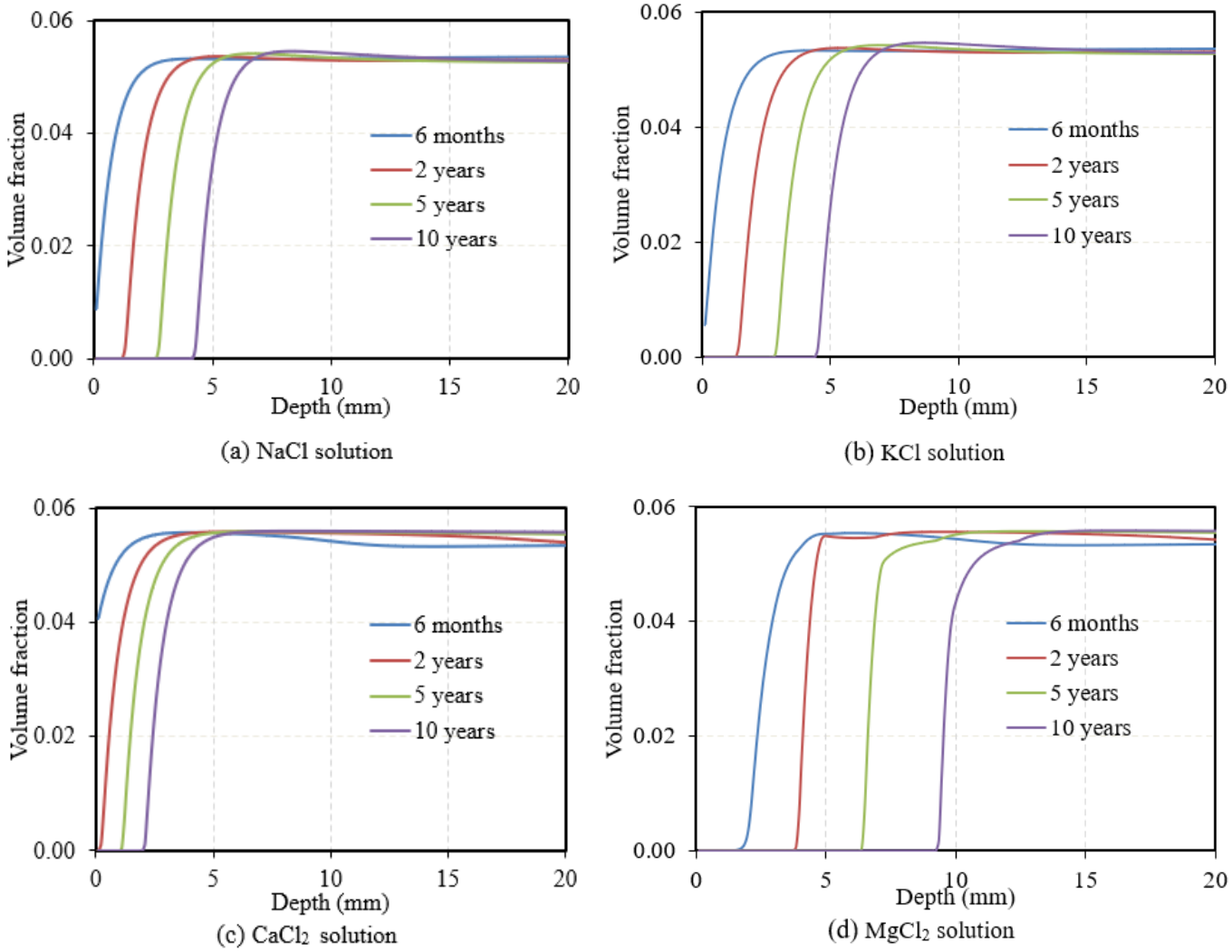

Figure 7. Portlandite volume fraction over depth of concrete exposed to different chloride solutions from 6 months to 10 years

Secondary Mg phases (Figure 13) reveal a distinct mechanism of deterioration. Sepiolite appears transiently at early ages, while brucite grows rapidly at the surface and later dissolves as the reaction front migrates inward. The formation of brucite and M-S-H corresponds to the pH reduction and porosity increase near the surface observed in Figures 5d-6d.

Overall, two regimes are evident. Monovalent systems (NaCl, KCl) are transport

controlled: hydration assemblages remain stable, chloride binding is moderate, and free chloride penetrates deeply. Divalent systems ($CaCl_2$, $MgCl_2$) are binding/microstructure-controlled: near-surface reactions form large chloride reservoirs (AFm, brucite, M-S-H) while reducing alkalinity and diffusivity. These mineralogical signatures explain the distinct chloride profiles and pH distributions reported earlier.

The predicted transformations align closely with the saturated-immersion experiments by De weerdt et al. [35] who also observed strong AFm formation under Ca^{2+} and extensive C-S-H decalcification under Mg^{2+}. They are also consistent with corrosion mechanisms summarized by Angst et al. [6], confirming that cation type controls whether chloride ingress is governed primarily by transport or by chemical fixation.

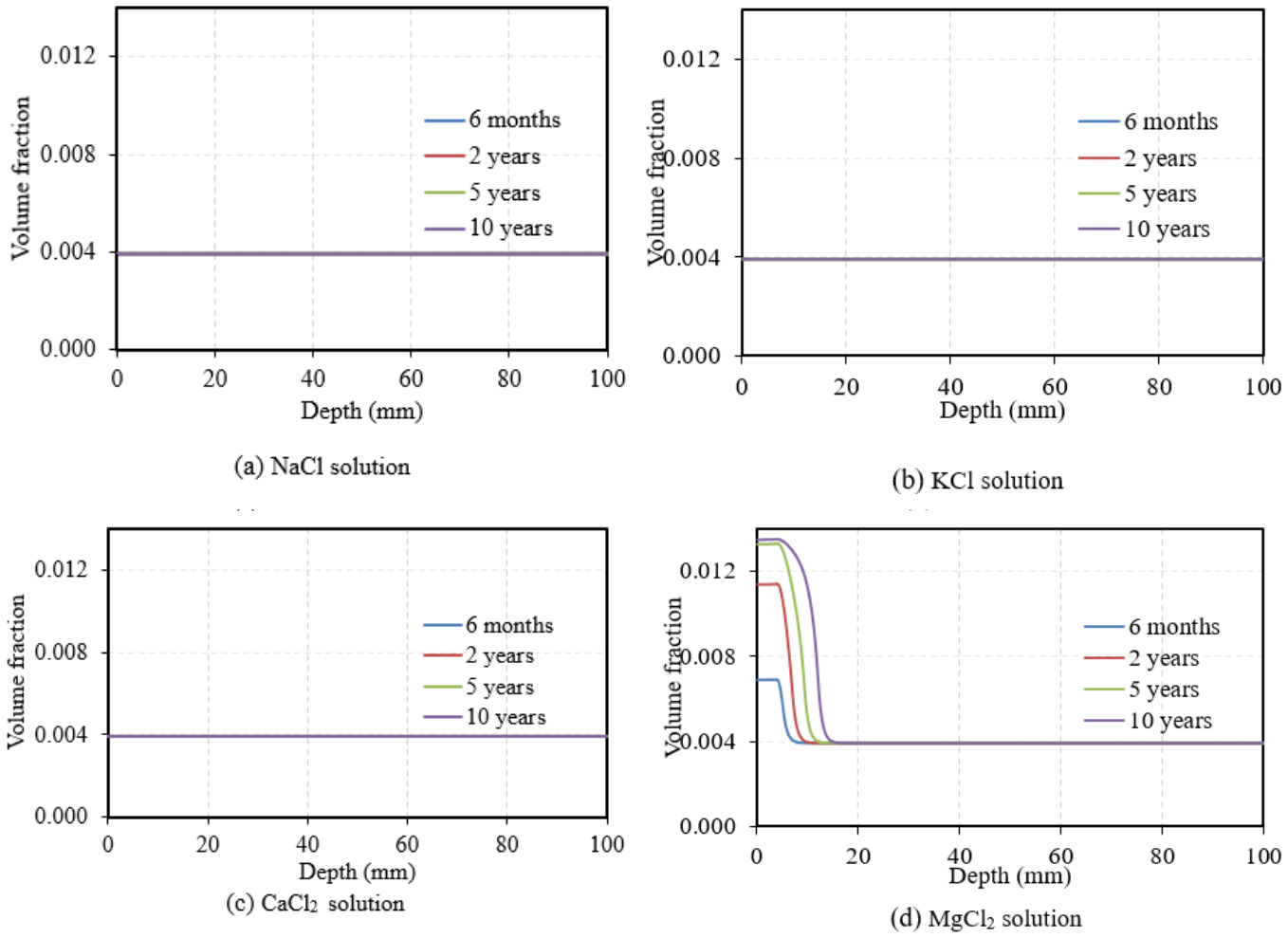

Figure 8. Hydrotalcite volume fraction over depth of concrete exposed to different chloride solutions from 6 months to 10 years

The model results show that the sensitivity to chloride exposure depends on the cation type and on the metric considered. For chloride ingress at cover depth, K^+ (and to a slightly lesser extent Na^+) is most critical, because limited phase change and preserved pore connectivity allow deep penetration of free Cl^-. For chloride binding near the surface, Ca^{2+} exerts the strongest effect by promoting the formation of chloride-bearing AFm phases and creating a large bound-chloride reservoir in the outer 5-15 mm. For hydrate stability and long-term microstructural damage, Mg^{2+} is the most aggressive cation: portlandite consumption and C-S-H decalcification lead to brucite/M-S-H formation, alkalinity loss, and gradual degradation of the cover. Thus, monovalent cations primarily control the depth of chloride ingress, while divalent cations mainly govern binding intensity and the

stability of the hydrate assemblage.

5. Conclusion

A reactive transport model was developed to simulate long-term chloride ingress in CEM II concrete exposed to four chloride solutions (NaCl, KCl, $CaCl_2$, $MgCl_2$) under saturated conditions. The model reproduced the experimental results of literature and revealed clear differences in transport and chemical behavior depending on the boundary cation.

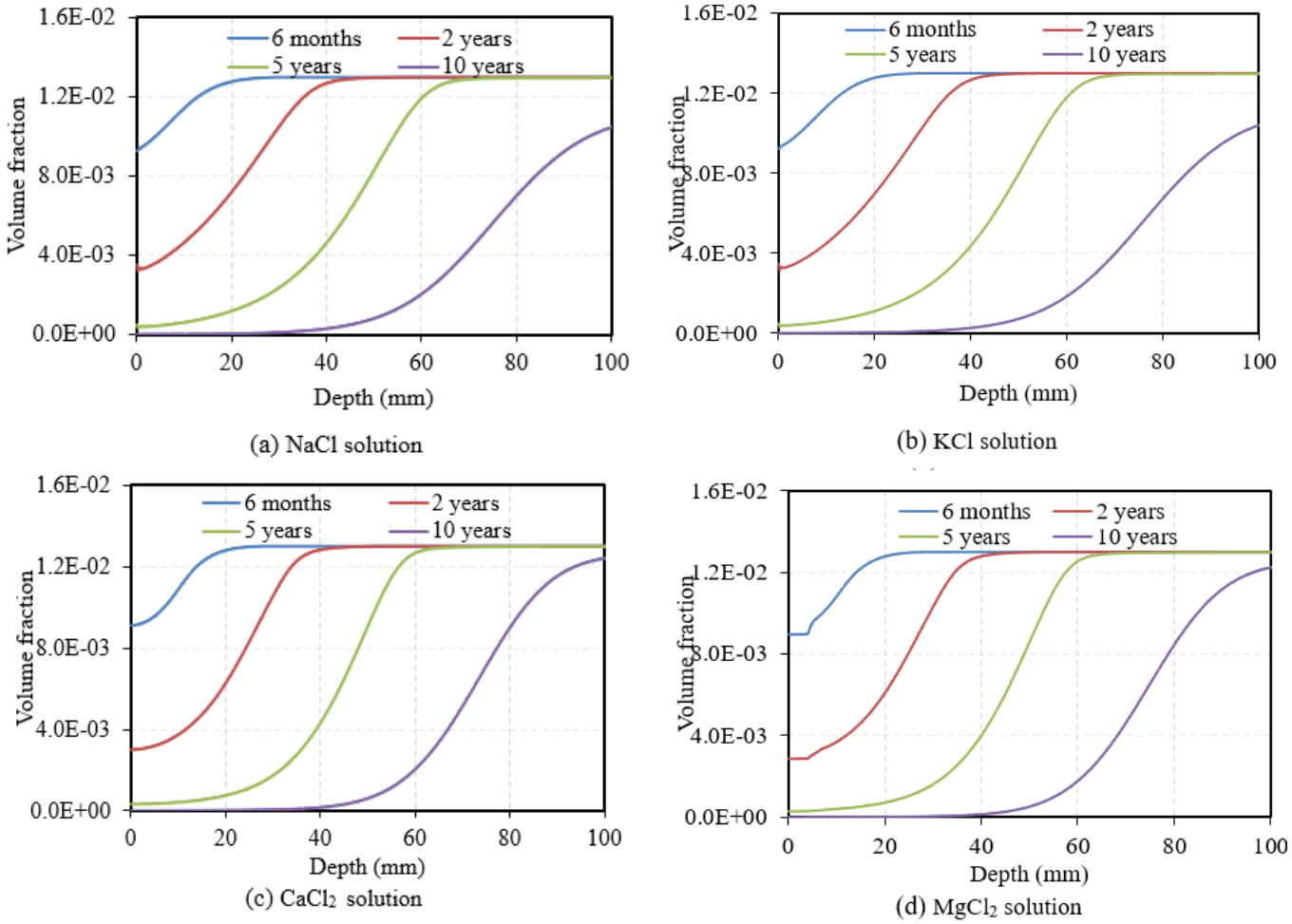

Figure 9. Monosulfoaluminate volume fraction over depth of concrete exposed to different chloride solutions from 6 months to 10 years

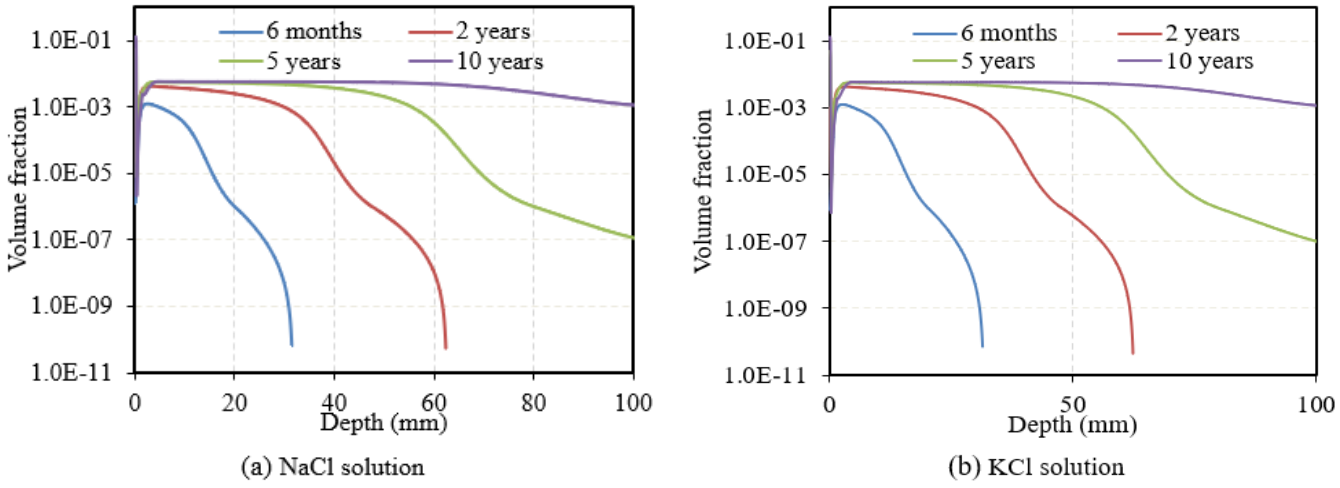

Figure 10. Ettringite volume fraction over depth of concrete exposed to different chloride solutions from 6 months to 10 years

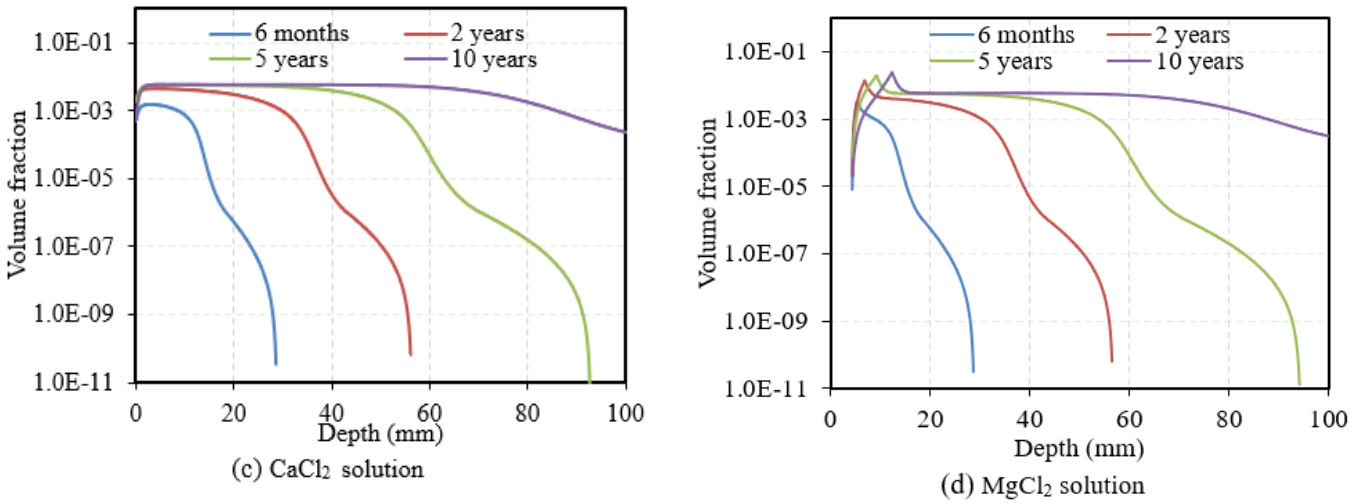

Figure 10. (continued)

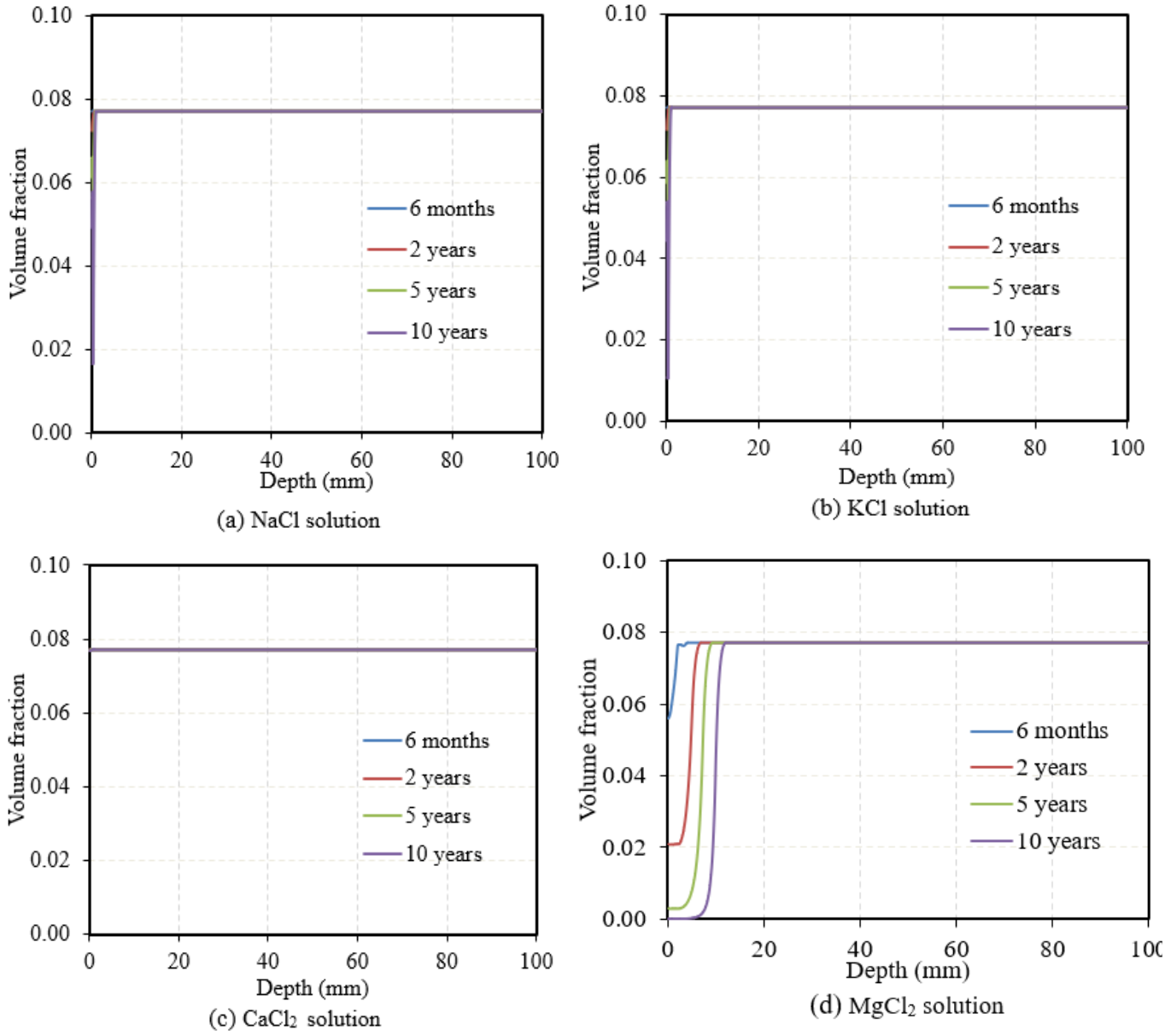

Figure 11. Jennite volume fraction over depth of concrete exposed to different chloride solutions from 6 months to 10 years

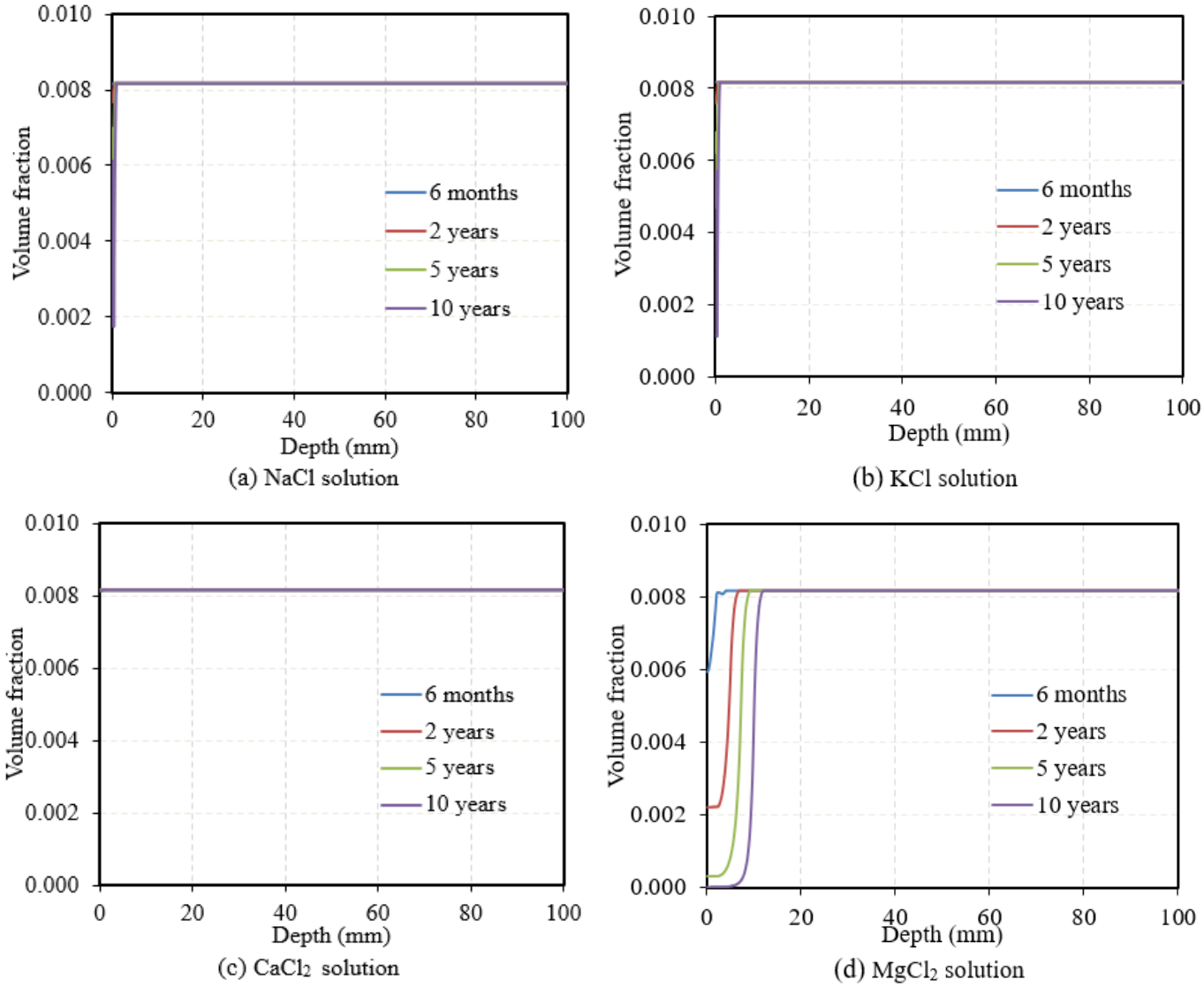

Figure 12. Tobermorite volume fraction over depth of concrete exposed to different chloride solutions from 6 months to 10 years

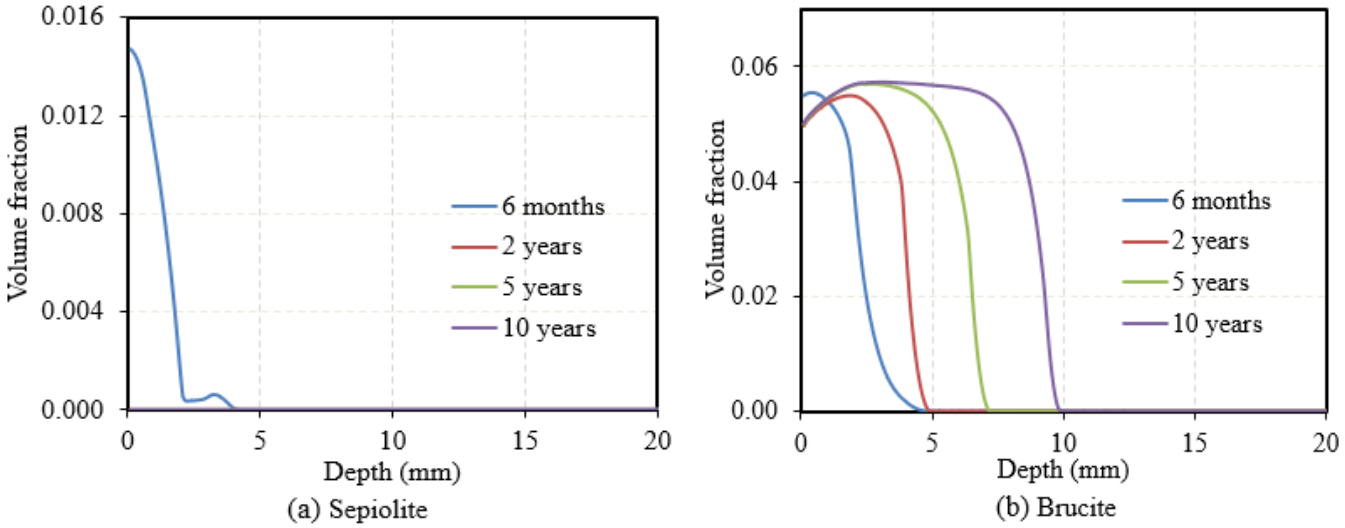

Figure 13. Volume fraction over depth of concrete exposed to magnesium chloride solution $MgCl_2$ from 6 months to 10 years

Monovalent systems (NaCl, KCl) showed a transport-controlled regime, where hydration phases remained stable, chloride binding was moderate, and free chloride penetrated deeply. Divalent systems ($CaCl_2$, $MgCl_2$) exhibited a binding/microstructure-controlled regime, marked by AFm transformation, portlandite consumption, and C-S-H decalcification that confined chloride near the surface. Using a practical free-chloride threshold of 0.04 g/100 g concrete, the 10-year penetration depth followed the order KCl ≈ NaCl > $CaCl_2$ > $MgCl_2$.

The pH and porosity fields confirmed that $MgCl_2$ caused the strongest near-surface alkalinity loss, while NaCl/KCl maintained a connected pore network that favored deeper transport. Phase-assemblage results (Figures 7-13) linked these patterns to the formation of chloride-bearing AFm ($CaCl_2$) and Mg-rich secondary phases (brucite, M-S-H) that alter the long-term binding capacity.

These findings demonstrate that chloride ingress is jointly governed by diffusion and mineral reactions. Performance-based durability design should therefore combine free chloride, total chloride, and pH evolution to assess corrosion initiation more accurately.

The present model assumes full saturation and constant temperature, without considering wet-dry cycles, mechanical damage, or chloride transport under coupled thermal-hydraulic-mechanical conditions. Future work should incorporate these coupled effects, validate kinetic parameters for high temperatures and blended binders, and extend the model to reinforced-concrete geometries for full corrosion-life prediction. The reactive transport model should be also be extended to unsaturated concrete with cyclic wetting-drying boundary conditions so that marine exposure can be represented more realistically.

Acknowledgement

This research is funded by Vietnam National Foundation for Science and Technology Development (NAFOSTED) under grant number 107.99-2023.16

Conflict of Interest: The authors declare that there is no conflict of interest.

Reference

[1] G.K. Glass, N.R. Buenfeld. (2000). The influence of chloride binding on the chloride induced corrosion risk in reinforced concrete. *Corrosion Science*, 42(2), 329-344. https://doi.org/10.1016/S0010-938X(99)00083-9

[2] V.Q. Tran, A. Soive, V. Baroghel-Bouny. (2018). Modelisation of chloride reactive transport in concrete including thermodynamic equilibrium, kinetic control and surface complexation. *Cement and Concrete Research*, 110, 70-85. https://doi.org/10.1016/j.cemconres.2018.05.007

[3] V.Q. Tran, V.L. Giap. (2022). Investigation in manufacturing self-healing cementitious materials using microbial technology. *Journal of Science and Transport Technology*, 2(2), 31-38. https://doi.org/10.58845/jstt.utt.2022.en.2.2.31-38

[4] V.Q. Tran, V.L. Giap, T.G. Nguyen. (2022). Investigating durability of concrete using geochemical model (Vietnamese). *Journal of Science and Transport Technology,* 2(4), 13-22. https://doi.org/10.58845/jstt.utt.2022.vn.2.4.13-22

[5] V.Q. Tran. (2016). Contribution to the Understanding of Reinforcement Depassivation Mechanisms in Concrete Exposed to Seawater: Theory and Thermochemical Modeling, Doctoral thesis (French). Ecole Centrale de Nantes.

[6] U.M. Angst. (2023). Steel corrosion in concrete – Achilles' heel for sustainable concrete? *Cement and Concrete Research*, 172, 107239. https://doi.org/10.1016/j.cemconres.2023.107239

[7] V.Q. Tran, A. Soive, S. Bonnet, A. Khelidj. (2018). A numerical model including thermodynamic equilibrium, kinetic control and surface complexation in order to explain cation

type effect on chloride binding capability of concrete. *Construction and Building Materials*, 191, 608-618. https://doi.org/10.1016/j.conbuildmat.2018.10.058

[8] T. Luping. (2008). Engineering expression of the ClinConc model for prediction of free and total chloride ingress in submerged marine concrete. *Cement and Concrete Research*, 38(8-9), 1092-1097. https://doi.org/10.1016/j.cemconres.2008.03.008

[9] V. Baroghel-Bouny, X. Wang, M. Thiery, M. Saillio, F. Barberon. (2012). Prediction of chloride binding isotherms of cementitious materials by analytical model or numerical inverse analysis. *Cement and Concrete Research*, 42(9), 1207-1224. https://doi.org/10.1016/j.cemconres.2012.05.008

[10] C. Song, C. Jiang, X.-L. Gu, Q. Zhang, W.-P. Zhang. (2022). Calibration analysis of chloride binding capacity for cement-based materials under various exposure conditions. *Construction and Building Materials*, 314, 125588. 10.1016/j.conbuildmat.2021.125588. https://doi.org/10.1016/j.conbuildmat.2021.125588

[11] T. Luping, L.-O. Nilsson. (1993). Chloride binding capacity and binding isotherms of OPC pastes and mortars. *Cement and Concrete Research*, 23(2), 247-253. https://doi.org/10.1016/0008-8846(93)90089-R

[12] L. Mao, L. Li, Y. Wang, Q. Liu. (2025). Physicochemical modelling in chlorides migration in concrete with account of multi-species coupling, reaction kinetic and pore evolution. *Construction and Building Materials*, 460, 139707. https://doi.org/10.1016/j.conbuildmat.2024.139707

[13] T. Matschei, B. Lothenbach, F.P. Glasser. (2007). Thermodynamic properties of Portland cement hydrates in the system CaO–Al2O3–SiO2–CaSO4–CaCO3–H2O. Cement and Concrete Research, 37(10), 1379-1410. https://doi.org/10.1016/j.cemconres.2007.06.002

[14] M. Balonis, B. Lothenbach, G.L. Saout, F.P. Glasser. (2010). Impact of chloride on the mineralogy of hydrated Portland cement systems. *Cement and Concrete Research*, 40(7), 1009-1022. https://doi.org/10.1016/j.cemconres.2010.03.002

[15] Z. Song, L. Jiang, J. Liu, J. Liu. (2015). Influence of cation type on diffusion behavior of chloride ions in concrete. *Construction and Building Materials*, 99, 150-158. https://doi.org/10.1016/j.conbuildmat.2015.09.033

[16] T. Li, H. Chen, L. Liu. (2025). Thermodynamic analysis of phase evolution in Portland cement paste exposed to NaCl and MgCl2 solutions: Concentration-dependent behavior and SCMs mitigation mechanism. *Construction and Building Materials*, 496, 143838. https://doi.org/10.1016/j.conbuildmat.2025.143838

[17] Z. Chen, H. Ye. (2023). Understanding the impact of main seawater ions and leaching on the chloride transport in alkali-activated slag and Portland cement. *Cement and Concrete Research*, 164, 107063. https://doi.org/10.1016/j.cemconres.2022.107063

[18] V.Q. Tran, H.-L. Nguyen, D.V. Dao, B. Hilloulin, L.K. Nguyen, Q.H. Nguyen, T.-T. Le, H.-B. Ly. (2020). Effect of temperature on the chloride binding capacity of cementitious materials. *Magazine of Concrete Research*, 73(15), 771-784. https://doi.org/10.1680/jmacr.19.00484

[19] V.Q. Tran. (2021). Using a geochemical model for predicting chloride ingress into saturated concrete. *Magazine of Concrete Research*, 74(6), 303-314.

https://doi.org/10.1680/jmacr.20.00424

[20] T. Xu, E. Sonnenthal, N. Spycher, K. Pruess. (2006). TOUGHREACT: A Simulation program for non-isothermal multiphase reactive geochemical transport in variably saturated geologic media: Applications to geothermal injectivity and CO2 geological sequestration. *Computers & Geosciences*, 32(2), 145-165. https://doi.org/10.1016/j.cageo.2005.06.014

[21] C.I. Steefel *et al.* (2015). Reactive transport codes for subsurface environmental simulation. *Computational Geosciences*, 19, 445-478. https://doi.org/10.1007/s10596-014-9443-x

[22] L. De Windt, F. Marsal, E. Tinseau, D. Pellegrini. (2008). Reactive transport modeling of geochemical interactions at a concrete/argillite interface, Tournemire site (France). *Physics and Chemistry of the Earth, Parts A/B/C*, 33, S295-S305. https://doi.org/10.1016/j.pce.2008.10.035

[23] C.I. Steefel, A.C. Lasaga. (1994). A coupled model for transport of multiple chemical species and kinetic precipitation/dissolution reactions with application to reactive flow in single phase hydrothermal systems. *American Journal of Science*, 294(5), 529–592. https://doi.org/10.2475/ajs.294.5.529

[24] A.C. Lasaga. (1998). Kinetic Theory in the Earth Sciences. Princeton series in Geochemistry. *Princeton University Press*.

[25] I. Baur, P. Keller, D. Mavrocordatos, B. Wehrli, C.A. Johnson. (2004). Dissolution-precipitation behaviour of ettringite, monosulfate, and calcium silicate hydrate. *Cement and Concrete Research*, 34(2), 341-348.https://doi.org/10.1016/j.cemconres.2003.08.016

[26] J.L. Palandri, Y.K. Kharaka. (2004). A compilation of rate parameters of water-mineral interaction kinetics for application to geochemical modeling. U.S. Geological Survey, 2004-1068, 2004. doi: https://doi.org/10.3133/ofr20041068

[27] Ph. Blanc, A. Lassin, P. Piantone, M. Azaroual, N. Jacquemet, A. Fabbri, E.C. Gaucher. (2012). Thermoddem: A geochemical database focused on low temperature water/rock interactions and waste materials. *Applied Geochemistry*, 27(10), 2107-2116. https://doi.org/10.1016/j.apgeochem.2012.06.002

[28] D.A. Kulik *et al.* (2013). GEM-Selektor geochemical modeling package: revised algorithm and GEMS3K numerical kernel for coupled simulation codes. *Computational Geosciences*, 17, 1-24. https://doi.org/10.1007/s10596-012-9310-6

[29] S. Galí, C. Ayora, P. Alfonso, E. Tauler, M. Labrador. (2001). Kinetics of dolomite–portlandite reaction: Application to portland cement concrete. *Cement and Concrete Research*, 31(6), 933-939. https://doi.org/10.1016/S0008-8846(01)00499-9

[30] V.Q. Tran. (2021). Using geochemical model for predicting chloride ingress into saturated concrete. *Magazine of Concrete Research*, 74(6), 303-314. https://doi.org/10.1680/jmacr.20.00424

[31] U. Angst, B. Elsener, C.K. Larsen, Ø. Vennesland. (2009). Critical chloride content in reinforced concrete — A review. *Cement and Concrete Research*, 39(12), 1122-1138. https://doi.org/10.1016/j.cemconres.2009.08.006

[32] M. Castellote, C. Andrade, C. Alonso. (1999). Chloride-binding isotherms in concrete submitted to non-steady-state migration experiments. *Cement and Concrete Research*, 29(11), 1799-1806. https://doi.org/10.1016/S0008-8846(99)00173-8

[33] Q. Zhu, L. Jiang, Y. Chen, J. Xu, L. Mo. (2012). Effect of chloride salt type on chloride binding behavior of concrete. *Construction and Building Materials*, 37, 512-517. https://doi.org/10.1016/j.conbuildmat.2012.07.079

[34] D.A. Hausmann. (1967). Steel corrosion in concrete -- How does it occur? *Materials Protection*, 6(11), 19-23.

[35] K. De Weerdt, D. Orsáková, M.R. Geiker. (2014). The impact of sulphate and magnesium on chloride binding in Portland cement paste. *Cement and Concrete Research*, 65, 30-40. https://doi.org/10.1016/j.cemconres.2014.07.007

[36] British Standards Institution. (2013). BS EN 206: 2013, Concrete – Specification, performance, production and conformity.